An extended element free Galerkin method for fracture analysis of functionally graded materials

Haider Khazal, Hamid Bayesteh, Soheil Mohammadi, Sayyed Shahram Ghorashi & Ameen Ahmed

Submit your article to this journal ↗

Article views: 30

View related articles ↗

View Crossmark data ↗

Taylor & Francis
Taylor & Francis Group

ORIGINAL ARTICLE

An extended element free Galerkin method for fracture analysis of functionally graded materials

Haider Khazal[a], Hamid Bayesteh[b], Soheil Mohammadi[b], Sayyed Shahram Ghorashi[c], and Ameen Ahmed[a]

[a]Mechanical Engineering Department, Basrah University, Basrah, Iraq; [b]School of Civil Engineering, University of Tehran, Tehran, Iran; [c]Faculty of Civil Engineering, Bauhaus-Universität Weimar, Weimar, Germany

ABSTRACT

An extended element free Galerkin method (XEFGM) has been adopted for fracture analysis of functionally graded materials (FGMs). Orthotropic enrichments functions are used along with the sub-triangle technique for enhancing the Gauss quadrature accuracy near the crack, and the incompatible interaction integral method is employed to calculate the stress intensity factors. Numerical simulations have proved that XEFGM provides more accurate results by less number of nodes (DOFs) in comparison with the unenriched EFGM and other conventional methods for several FGM problems with different crack locations and loadings. The results have been compared with the reference results, showing the reliability, stability, and efficiency of present XEFGM.

1. Introduction

Today, functionally graded materials (FGMs) are significant in many branches of engineering applications, including aerospace, automobile, medical equipment, turbine industries, etc. A formulated concept of FGMs was proposed in 1984 by material scientists in Sendai, Japan, as a means of preparing thermal barrier materials, and was followed by a coordinated research in that country since 1986. The idea of continuously changing the composition, microstructure, porosity, etc. of these materials, which results in gradients in various properties such as mechanical strength and thermal conductivity, has spread all over the world in recent years [1]. FGMs are gradually replacing layered composites in different applications from high-tech industries to rather ordinary devices.

Several studies have been performed on fracture analysis of functionally graded materials. Most of the studies on these types of materials have been conducted by using the numerical methods rather than the theoretical methods due to inability to analytically investigate such complicated problems. In calculation of the stress intensity factors in isotropic FGMs, the order of singularity of the stress field in the vicinity of the crack tip was assumed the same as isotropic homogenous materials [2]. Dolbow and Gosz [3] presented an approach that was applicable to analysis of FGMs in which the form of the asymptotic near-tip fields matched those of a homogeneous material. In the derivation, an interaction energy contour integral was expressed in the domain form and evaluated as a post processing step in the extended finite element method (XFEM). Rao and Rahman [4] used the meshless element free Galerkin method (EFGM) for calculating the fracture parameters of isotropic FGM by developing two interaction integrals in terms of homogenous and nonhomogenous

auxiliary fields. In addition, Kim and Paulino [5] developed an accurate scheme for evaluating mixed-mode stress intensity factors (SIFs) by means of the interaction integral (M-integral) within a finite element method (FEM) considering arbitrarily oriented straight and curved cracks in two-dimensional (2D) orthotropic FGMs. The interaction integral proved to be an accurate and robust scheme in the numerical problems where various types of material gradation, such as exponential, radial, and hyperbolic-tangent, might exist. They observed that the material orthotropy, material gradation, and the direction of material gradation could have a significant influence on SIFs. Also, Kim and Paulino [6] provided a critical assessment and comparison of three different formulations: non-equilibrium, incompatibility, and constant-constitutive-tensor formulations for calculation of stress intensity factor in FGMs by the interaction integral approach.

Dai et al. [7] used a mesh-free model for the static and dynamic analyses of FGM plates based on the radial point interpolation method (PIM). In this method, the mid-plane of FGM plate was represented by a set of distributed nodes while the material properties across the thickness were computed analytically to take into account their continuous variations from one surface to another. Sladek et al. [8] used a meshless local boundary integral equation method for a dynamic anti-plane shear crack problem in functionally graded materials. In addition, Gao et al. [9] presented 2D crack analysis in nonhomogeneous isotropic and linear elastic FGMs by a boundary-domain integral formulation. Developments in the extended finite element method have enormously contributed in fracture analysis of complex materials, such as composites and FGMs. Asadpoure et al, [10, 11] presented a modeling crack in orthotropic media using coupled finite element and partition of unity
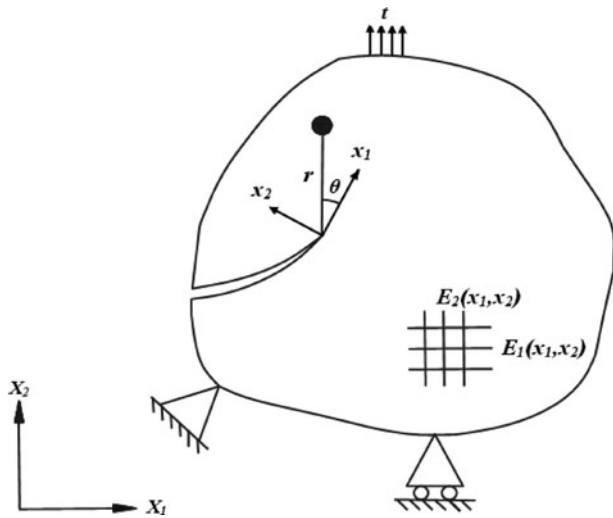

Figure 1. A cracked orthotropic FGM body.

methods. Motamedi and Mohammadi [12–14] studied the dynamic behavior of fixed and moving cracks in orthotropic media using the extended finite element method. Also, delamination analysis of composites by new orthotropic bimaterial extended finite element method was performed by Esna Ashari and Mohammadi [15]. Similarly, Ghorashi et al. [16] presented a novel extended isogeometric analysis (XIGA) approach based on the combination of isogeometric analysis (IGA) and extended FEM for fracture analysis of structures. Recently, XFEM fracture analysis of orthotropic functionally graded materials with orthotropic crack tip enrichments was reported by Bayesteh and Mohammadi [17], Hosseini et al. [18], and Goli et al. [19] to solve thermodynamic crack propagation of isotropic and anisotropic functionally graded materials.

One of the well-developed mesh-free methods is the element free Galerkin (EFG) method [20–24], which is adopted in this work. An enriched form of EFG is also available for crack analysis, which has the major advantages of capability solving several crack length/orientation problems on a fixed nodal distribution and no redistribution/remeshing is necessary even for crack propagation problems [25]. EFG provides a number of other

major advantages [26, 27], including higher accuracy, adaptive handling of large deformations, higher-order of continuity, and a relatively high stability solution. EFGM uses the moving least squares (MLS) approximation for generating the shape functions of required order of continuity. This feature of MLS approximation has allowed for it to be used in complicated problems and in the form of strong and weak formulations.

Similarly, MLS approximation was used to construct the shape functions in meshless local Petrov–Galerkin method (MLPG), developed by Atluri et al [28–30], where no global background mesh was required. Recently, Viola et al. [31, 32] presented the generalized differential quadrature finite element method (GDQFEM) for modeling of composite structures and compared their results with the cell method (CM) and FEM. Alternative approaches [33, 34] were also introduced for composite materials based on either the moving least-square approximation or the PIM.

Being free from the restrictions of mesh-based methods, such as FEM, EFG can be used more efficiently to solve complicated problems, such as discontinuities, considerable meshings, and remeshings practices in structural optimization problems, or having multi domains of influence in multi physics problems. It is very difficult and sometimes impossible to completely overcome those mesh-related difficulties by a mesh-based method [35]. In this study, the development of extended EFGM for fracture analysis of cracked isotropic and orthotropic FGMs is presented. The sub-triangular technique near the crack tip, modified support domain in the location of the crack tip, effective nodal distribution for the local crack region and for the whole geometry, and interaction integral method (M-integral) with the incompatibility form to calculate SIFs are explained in detail. Several case studies are considered and the results are verified with those available in the literature to assess the accuracy and the efficiency of the proposed extended element free Galerkin method for fracture analysis of orthotropic FGMs.

2. Constitutive equations

The Hooke's law for 2D elastic solids has the following form:

$$\sigma = \mathbf{D}\varepsilon, \tag{1}$$

where $\mathbf{D}$ is the matrix of material constants.

For isotropic nonhomogenous materials (FGMs), $\mathbf{D}$ can be defined as:

$$\mathbf{D} = \frac{E(x)}{1-\nu^2} \begin{bmatrix} 1 & \nu(x) & 0 \\ \nu & 1 & 0 \\ 0 & 0 & (1-\nu(x))/2 \end{bmatrix} \quad \text{(Plane stress)} \tag{2}$$

and

$$\mathbf{D} = \frac{E(x)(1-\nu(x))}{(1+\nu(x))(1-2\nu(x))}$$
$$\times \begin{bmatrix} 1 & \frac{\nu(x)}{1-\nu(x)} & 0 \\ \frac{\nu(x)}{1-\nu(x)} & 1 & 0 \\ 0 & 0 & \frac{1-2\nu(x)}{2(1-\nu(x))} \end{bmatrix} \quad \text{(Plane strain)}. \tag{3}$$

$E(x)$ and $\upsilon(x)$ in Eqs. (2) and (3) can be viewed as smoothly varying "effective" material properties of FGMs. This change in
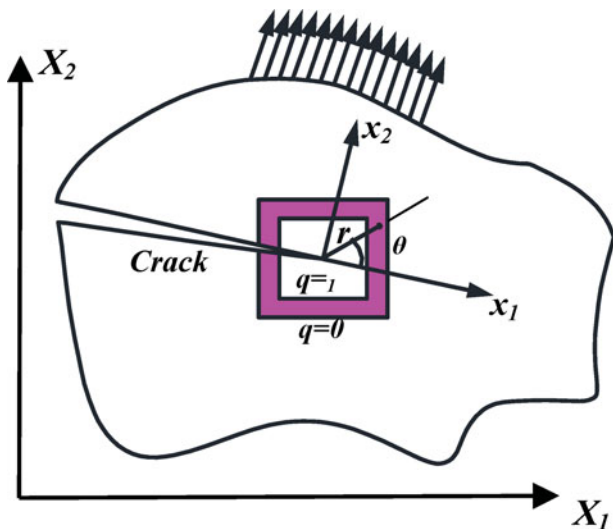

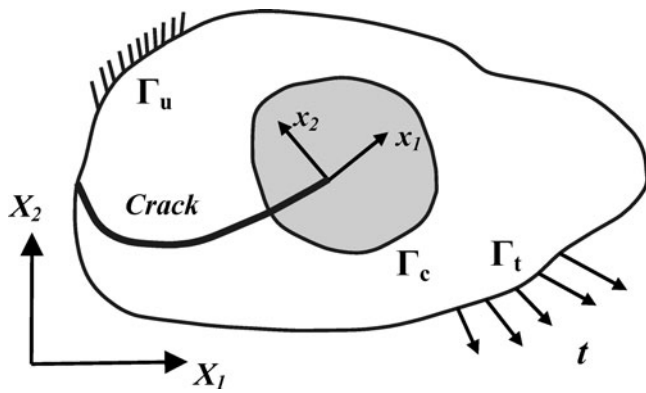**Figure 2.** The contour integral at the crack tip.

Figure 3. A general 2D cracked body.

the material properties cannot be easily implemented in analysis of anisotropic materials by many existing numerical methods.

For isotropic materials in the plane stress state, Eq. (1) can be converted to:

$$\varepsilon = \mathbf{C}\sigma = \begin{bmatrix} c_{11} & c_{12} & c_{16} \\ c_{12} & c_{22} & c_{26} \\ c_{16} & c_{26} & c_{66} \end{bmatrix} \begin{Bmatrix} \sigma_{xx} \\ \sigma_{yy} \\ \sigma_{xy} \end{Bmatrix}, \tag{4}$$

where $\mathbf{C}$ is the compliance matrix. $\mathbf{C}$ for orthotropic plane stress problems can be written as:

$$\mathbf{C} = \begin{bmatrix} \frac{1}{E_1} & -\frac{\nu_{12}}{E_1} & 0 \\ -\frac{\nu_{12}}{E_1} & \frac{1}{E_2} & 0 \\ 0 & 0 & \frac{1}{G_{12}} \end{bmatrix}. \tag{5}$$

3. Crack tip asymptotic solution

Figure 1 defines a 2D orthotropic cracked body subjected to typical forces with relevant boundary condition, and definitions of global, local, and polar coordinates. The characteristic equation, obtained from the equilibrium and compatibility, can be written as [36, 37]:

$$c_{11}s^4 - 2c_{16}s^3 + (2c_{12} + c_{66})s^2 - 2c_{26}s + c_{22} = 0, \tag{6}$$

where c_{ij} are the components of the compliance matrix $\mathbf{C}$.

The 2D displacement and stress fields in the vicinity of the crack tip are defined in terms of the roots $s_k = s_{kx} + is_{ky}$, $k = 1, 2$ [36, 38]:
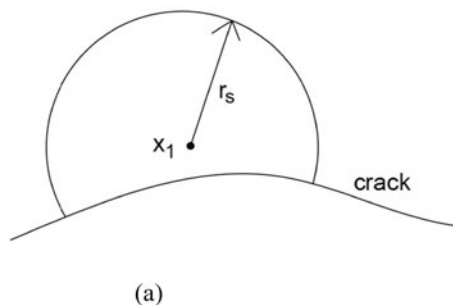
3.1. Mode I

$$u_1^{\mathrm{I}} = K_I \sqrt{\frac{2r}{\pi}} \mathrm{Re} \left[\frac{1}{s_1 - s_2} \left(s_1 p_2 \sqrt{\cos\theta + s2\sin\theta} \right. \right.$$
$$\left. \left. - s_2 p_1 \sqrt{\cos\theta + s_1\sin\theta} \right) \right], \tag{7}$$

$$u_2^{I} = K_I \sqrt{\frac{2r}{\pi}} \mathrm{Re} \left[\frac{1}{s_1 - s_2} \left(s_1 q_2 \sqrt{\cos\theta + s_2\sin\theta} \right. \right.$$
$$\left. \left. - s_2 q_1 \sqrt{\cos\theta + s_1\sin\theta} \right) \right], \tag{8}$$

$$\sigma_{xx}^{I} = \frac{K_I}{\sqrt{2\pi r}} \mathrm{Re} \left[\frac{s_1 s_2}{s_1 - s_2} \left(\frac{s_2}{\sqrt{\cos\theta + s_2\sin\theta}} \right. \right.$$
$$\left. \left. - \frac{s_1}{\sqrt{\cos\theta + s_1\sin\theta}} \right) \right], \tag{9}$$

$$\sigma_{yy}^{I} = \frac{K_I}{\sqrt{2\pi r}} \mathrm{Re} \left[\frac{1}{s_1 - s_2} \left(\frac{s_1}{\sqrt{\cos\theta + s_2\sin\theta}} \right. \right.$$
$$\left. \left. - \frac{s_2}{\sqrt{\cos\theta + s_1\sin\theta}} \right) \right], \tag{10}$$

$$\sigma_{xy}^{I} = \frac{K_I}{\sqrt{2\pi r}} \mathrm{Re} \left[\frac{s_1 s_2}{s_1 - s_2} \left(\frac{1}{\sqrt{\cos\theta + s_1\sin\theta}} \right. \right.$$
$$\left. \left. - \frac{1}{\sqrt{\cos\theta + s_2\sin\theta}} \right) \right]. \tag{11}$$

3.2. Mode II

$$u_1^{II} = K_{II} \sqrt{\frac{2r}{\pi}} \mathrm{Re} \left[\frac{1}{s_1 - s_2} \left(p_2 \sqrt{\cos\theta + s_2\sin\theta} \right. \right.$$
$$\left. \left. - p_1 \sqrt{\cos\theta + s_1\sin\theta} \right) \right], \tag{12}$$

$$u_2^{II} = K_{II} \sqrt{\frac{2r}{\pi}} \mathrm{Re} \left[\frac{1}{s_1 - s_2} \left(q_2 \sqrt{\cos\theta + s_2\sin\theta} \right. \right.$$
$$\left. \left. - q_1 \sqrt{\cos\theta + s_1\sin\theta} \right) \right], \tag{13}$$
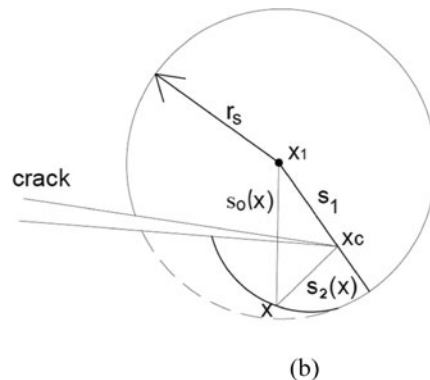

(a)

(b)

Figure 4. Selection of the support domain: (a) near a crack face and (b) near a crack tip (r_s: radius of support domain).
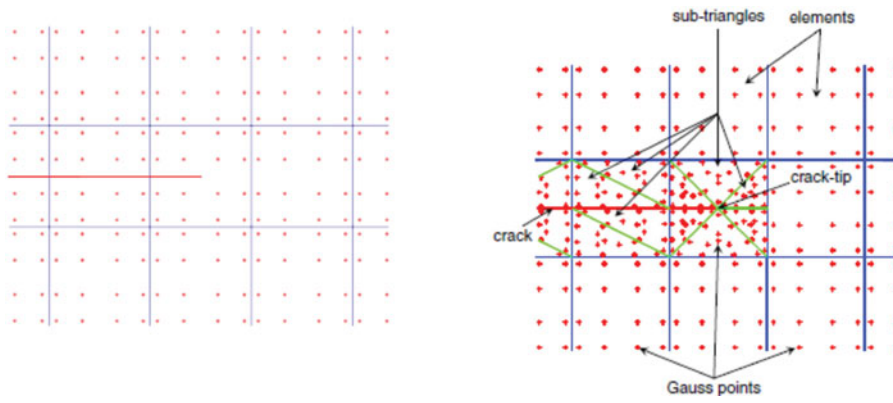
Figure 5. Distribution of Gauss points around the crack in the standard approach and the sub-triangles technique.

$$\sigma_{xx}^{II} = \frac{K_{II}}{\sqrt{2\pi r}} \text{Re} \left[\frac{1}{s_1 - s_2} \left(\frac{s_2^2}{\sqrt{\cos\theta + s_2\sin\theta}} - \frac{s_1^2}{\sqrt{\cos\theta + s_1\sin\theta}} \right) \right], \tag{14}$$

$$\sigma_{yy}^{II} = \frac{K_{II}}{\sqrt{2\pi r}} \text{Re} \left[\frac{1}{s_1 - s_2} \left(\frac{1}{\sqrt{\cos\theta + s_2\sin\theta}} - \frac{1}{\sqrt{\cos\theta + s_1\sin\theta}} \right) \right], \tag{15}$$

$$\sigma_{xy}^{II} = \frac{K_{II}}{\sqrt{2\pi r}} \text{Re} \left[\frac{1}{s_1 - s_2} \left(\frac{s_1}{\sqrt{\cos\theta + s_1\sin\theta}} - \frac{s_2}{\sqrt{\cos\theta + s_2\sin\theta}} \right) \right], \tag{16}$$

where Re represents the real part of the statement, K_I and K_{II} are the stress intensity factors for mode I and mode II, respectively, and p_i and q_i are defined as:

$$p_i = c_{11}s_i^2 + c_{12} - c_{16}s_i \quad i = 1, 2, \tag{17}$$

$$q_i = c_{12}s_i + \frac{c_{22}}{s_i} - c_{26} \quad i = 1, 2 \tag{18}$$

In FGMs (Figure 1), the material properties, such as the modulus of elasticity E and the Poisson's ratio ν, vary in different points of the domain. Nevertheless, due to the fact that the linear-elastic singular stress field near the crack tip cannot be
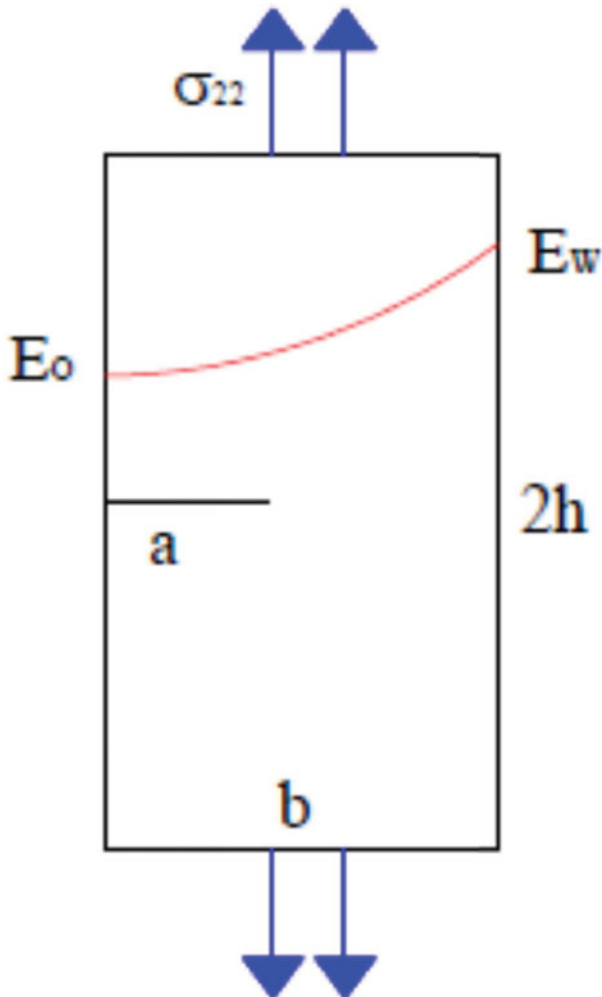

Figure 6. An edge crack parallel to the material gradation in a rectangular functionally graded plate subjected to unit tensile loading.
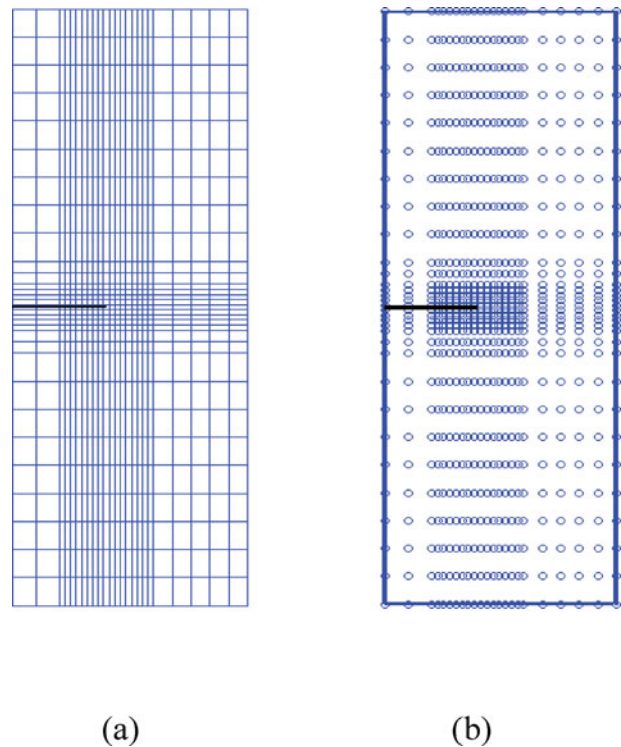

(a)   (b)

Figure 7. Background cells and nodal distribution for modeling the rectangular functionally graded plate.
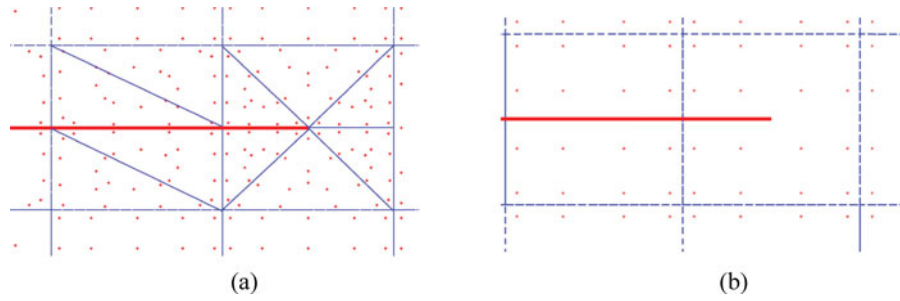
Figure 8. Gauss points around the crack: (a) sub-triangles technique and (b) conventional (ordinary) distribution.

analytically obtained for general FGM problems, it is common to assume that the field functions are similar to homogenous media based on the crack tip material properties [4]. Similarly, the displacements and stresses of a cracked orthotropic FGM are obtained from Eqs. (7)–(18) by calculating the roots of the characteristic equation (6) at the crack tip.

4. Computation of stress intensity factors by the interaction integral

Various forms of the interaction integral have been used to obtain the SIFs, including the nonequilibrium, the incompatibility, and the constant-constitutive-tensor formulations, as proposed by Kim and Paulino [6]. In the present work, the incompatibility formulation is employed to approximate the J-integral because it requires less complicated derivatives with more or less the same level of accuracy as the nonequilibrium formulation [6, 18]. The incompatibility formulation is based on the following relations for the auxiliary fields:

$$\sigma_{ij} = d_{ijkl}(x)\,\varepsilon_{kl}, \varepsilon_{ij} \neq \frac{1}{2}\left(u_{i,j} + u_{j,i}\right), \sigma_{ij,j} = 0 \quad (19)$$

where d_{ijkl} is the material modulus. The material compliance tensor c_{ijkl} can be obtained from the first relation of Eq. (19):

$$\varepsilon_{ij} = c_{ijkl}(x)\,\sigma_{kl} \quad (i, j, k, l = 1, 2, 3). \quad (20)$$

Coefficients c_{ijkl} are related to components of the material compliance matrix c_{ij}:

$$\begin{bmatrix} c_{11} & c_{12} & c_{16} \\ c_{12} & c_{22} & c_{26} \\ c_{16} & c_{26} & c_{66} \end{bmatrix} = \begin{bmatrix} c_{1111} & c_{1122} & 2c_{1112} \\ c_{2211} & c_{2222} & 2c_{2212} \\ 2c_{1211} & 2c_{1222} & 4c_{1212} \end{bmatrix}. \quad (21)$$

Table 1. Comparison of SIFs with [9] for $r_J = 0.5$ and $r_J = 0.6$.

		XEFG Normalized K_I $r_J = 0.5$		XEFG Normalized K_I $r_J = 0.6$	
αb	Normalized KI [9]	Value	Error%	Value	Error%
1.6	1.741	1.769	1.60	1.753	0.69
1.199	1.824	1.853	1.58	1.837	0.71
0.8	1.909	1.931	1.15	1.918	0.47
0.399	1.992	2.008	0.80	1.998	0.30
0	2.073	2.082	0.43	2.075	0.09
−0.399	2.150	2.152	0.09	2.149	0.04
−0.8	2.222	2.216	0.27	2.222	0
−1.199	2.291	2.281	0.43	2.291	0
−1.6	2.353	2.344	0.38	2.356	0.12

The equivalent domain formulation of the J-integral for an arbitrary contour Γ surrounding the crack tip can be expressed as (Figure 2):

$$J = \int_A \left(\sigma_{ij}u_{i,1} - w\delta_{1j}\right) q_{,j}dA + \int_A \left(\sigma_{ij}u_{i,1} - w\delta_{1j}\right)_{,j} qdA, \quad (22)$$

where q is a smooth function varying from $q = 1$ on the interior boundary of surface A to $q = 0$ on the outer one. n_j is the jth component of the outward unit normal to Γ, δ_{ij} is the Kronecker delta and the local Cartesian coordinate system x_1 is set parallel to the crack surface. w is the strain energy density:

$$w = \frac{1}{2}\sigma_{ij}\varepsilon_{ij}. \quad (23)$$

The interaction integral method is applied to calculate the mode I and II stress intensity factors. The interaction integral can be defined as [39, 40]:

$$M = \int_A \left\{\sigma_{ij}u_{i,1}^{aux} + \sigma_{ij}^{aux}u_{i,1} - \frac{1}{2}\left(\sigma_{ik}\varepsilon_{ik}^{aux} + \sigma_{ik}^{aux}\varepsilon_{ik}\right)\delta_{1j}\right\} q_{,j}dA$$
$$+ \int_A \left\{\sigma_{ij}\left(c_{ijkl}^{tip} - c_{ijkl}(x)\right)\sigma_{kl,1}^{aux}\right\} qdA. \quad (24)$$

The effect of two superimposed fields can be written as [37, 38]:

$$M = 2t_{11}K_I^{aux}K_I + t_{12}\left(K_I^{aux}K_{II} + K_{II}^{aux}K_I\right) + 2t_{22}K_{II}^{aux}K_{II}, \quad (25)$$

with

$$t_{11} = -\frac{c_{11}}{2}Im\left(\frac{s_1 + s_2}{s_1 s_2}\right), \quad (26)$$

$$t_{12} = -\frac{c_{22}}{2}Im\left(\frac{1}{s_1 s_2}\right) + \frac{c_{11}}{2}Im\left(s_1 s_2\right), \quad (27)$$

$$t_{22} = -\frac{c_{11}}{2}Im\left(s_1 + s_2\right). \quad (28)$$

Substituting $K_I^{aux} = 1, K_{II}^{aux} = 0$ and $K_I^{aux} = 0, K_{II}^{aux} = 1$ into Eq. (25), results in the following simplified simultaneous equations:

$$\begin{aligned} M_1 &= 2t_{11}K_I + t_{12}K_{II} \quad (K_I^{aux} = 1, K_{II}^{aux} = 0), \\ M_2 &= t_{12}K_I + 2t_{22}K_{II} \quad (K_I^{aux} = 0, K_{II}^{aux} = 1), \end{aligned} \quad (29)$$

which should be solved for calculation of the actual modes I and II stress intensity factors.
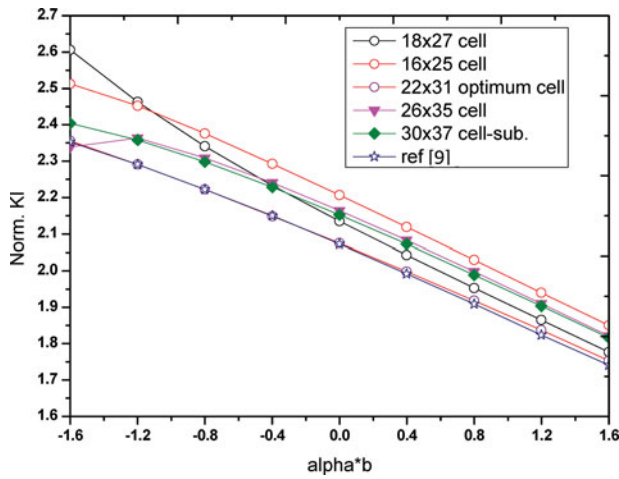
Figure 9. Different background cells compared with [9].

5. EFG formulation

Figure 3 shows a 2D problem of linear elasticity, which includes a crack Γ_c. The partial differential equation of this problem can be written in the form of:

$$\text{Equilibrium equation}: \boldsymbol{L}^T\boldsymbol{\sigma}$$
$$+b = 0 \text{ in problem domain } \Omega, \tag{30}$$

with the following boundary conditions:

$$\text{Natural boundary condition}: \boldsymbol{\sigma}n = \bar{\boldsymbol{t}} \text{ on } \Gamma_t, \tag{31}$$

$$\text{Essential boundary condition}: \boldsymbol{u} = \bar{\boldsymbol{u}} \text{ on } \Gamma_u, \tag{32}$$
$$\text{Traction freecrack}: \boldsymbol{\sigma}n = 0 \text{ on } \Gamma_c, \tag{33}$$

where $\boldsymbol{L}$ is the differential operator defined as:

$$L = \begin{bmatrix} \frac{\partial}{\partial x} & 0 \\ 0 & \frac{\partial}{\partial y} \\ \frac{\partial}{\partial y} & \frac{\partial}{\partial x} \end{bmatrix}, \tag{34}$$
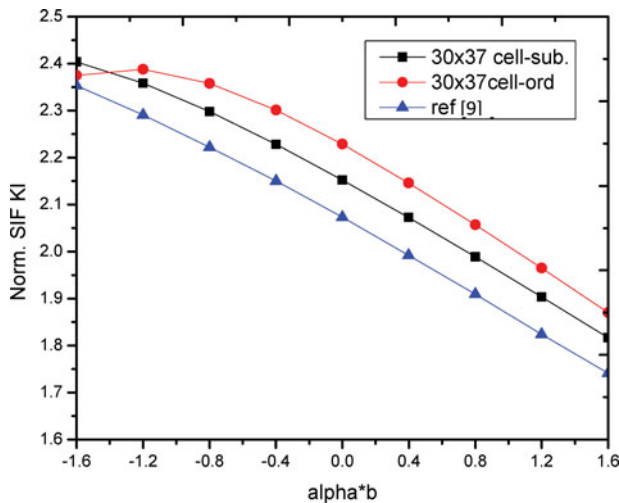

Figure 10. Sub-triangular and ordinary techniques compared with [9] for the finest background mesh.
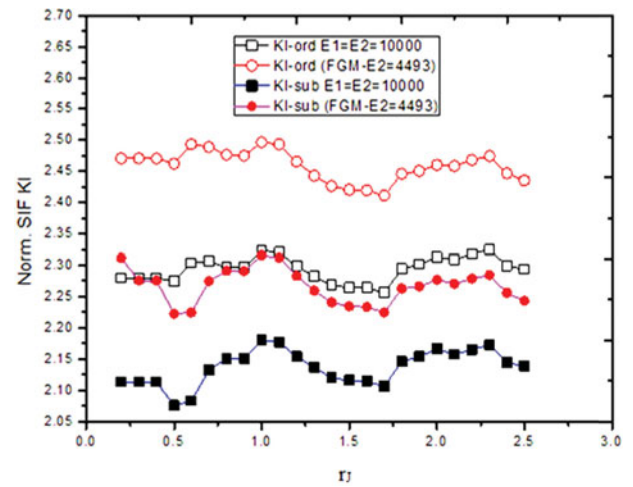

Figure 11. Values of SIFs for various relative r_J for the case of 22×31 background mesh.

and $\boldsymbol{\sigma}$, u, and $\boldsymbol{b}$ are the stress, displacement, and body force vectors, respectively. $\bar{\boldsymbol{t}}$ is the prescribed traction on the traction (natural) boundary; $\bar{\boldsymbol{u}}$ is the prescribed displacement on the displacement (essential) boundary; and n is the unit outward normal vector at a point on the natural boundary.

Since the MLS shape functions lack the Kronecker delta function property, the Lagrange multiplier technique is adopted to enforce the essential (displacement) boundary conditions. The constrained weak form of the governing equation can be written as:

$$\int_{\Omega} (\boldsymbol{L}\delta u)^T (\boldsymbol{D}Lu) \, d\Omega - \int_{\Omega} \delta \boldsymbol{u}^T b d\Omega - \int_{\Gamma_t} \delta \boldsymbol{u}^T \bar{\boldsymbol{t}} d\Gamma$$
$$- \int_{\Gamma_u} \delta \boldsymbol{\lambda}^T (u - \bar{u}) \, d\Gamma - \int_{\Gamma_u} \delta \boldsymbol{u}^T \lambda d\Gamma = 0, \tag{35}$$

where $\boldsymbol{D}$ is the matrix of elastic constants (inverse of compliance matrix $\boldsymbol{c}$), and $\boldsymbol{\lambda}$ is the Lagrange multiplier variable.

The problem domain is now represented by a set of n field nodes in order to approximate the displacement variable. EFG uses the moving least squares (MLS) shape functions [41] to approximate the displacement at any point of interest using a set of nodes in the local support domain of that point. The MLS shape function associated with the node i and point $\boldsymbol{x}$ can be written as [42]:

$$\phi_i(\boldsymbol{x}) = \boldsymbol{p}^T(x) [A(x)]^{-1} w(\boldsymbol{x} - \boldsymbol{x}_i) \boldsymbol{p}(x_i), \tag{36}$$

Table 2. The error in SIFs for different number of Gauss points in each sub-triangle.

αb	Error % (7 Gauss points)	Error % (13 Gauss points)
1.6	1.03	0.69
1.199	1.06	0.71
0.8	0.90	0.47
0.399	1.36	0.30
0	0.56	0.09
−0.399	0.34	0.04
−0.8	0.03	0.00
−1.199	0.97	0.00
−1.6	2.80	0.12
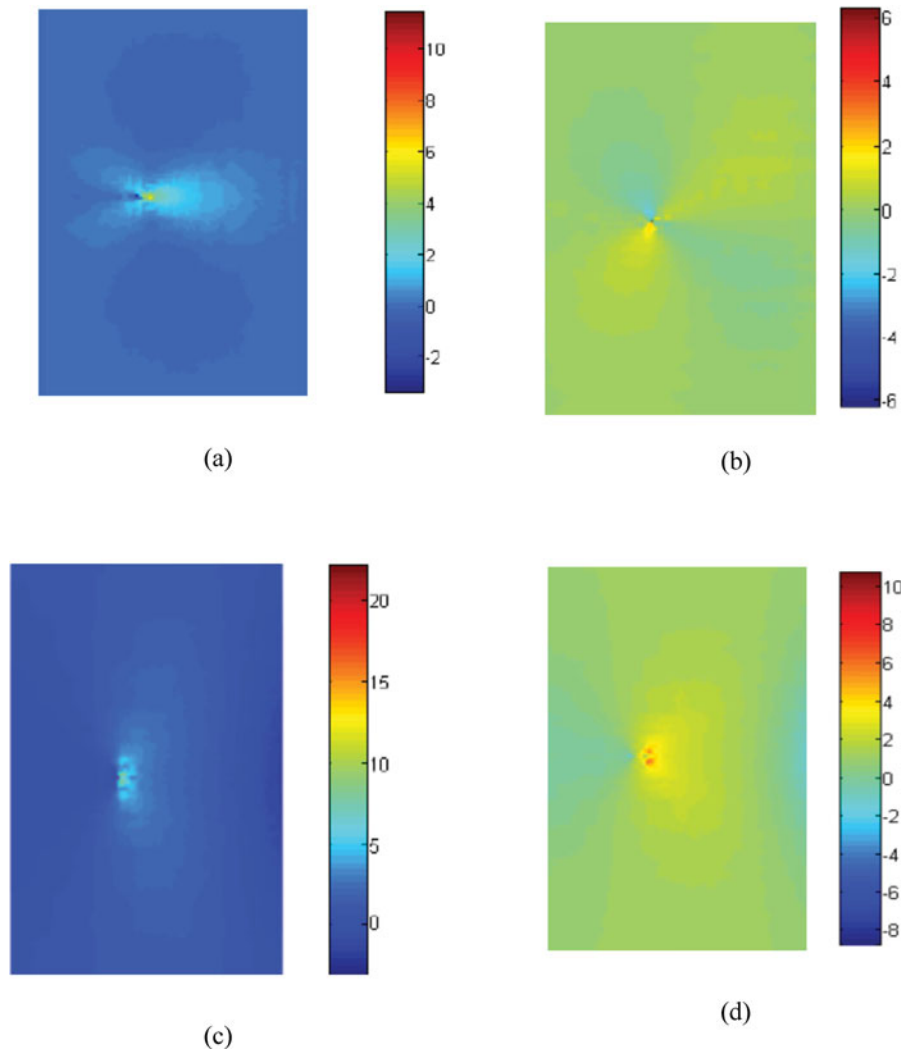
Figure 12. Contours of stress components around the crack tip: (a)–(c) enriched σ_{xx}, σ_{xy}, and σ_{yy}, respectively, and (d) σ_{yy} without enrichment functions. ($\alpha b = 1.6$, $r_J =$ 0.5, $d_{max} = 1.7$, 752 field nodes, 13 gauss points for each sub-triangle). Units of stress are MPa.

where $\boldsymbol{p}(x)$ is the basis function. A linear basis function is adopted in this study:

$$\boldsymbol{p}^T(\boldsymbol{x}) = \begin{bmatrix} 1 & x & y \end{bmatrix}, \tag{37}$$

and $\boldsymbol{A}$ is defined as:

$$\boldsymbol{A}(\boldsymbol{x}) = \sum_{i=1}^{n} w(\boldsymbol{x} - \boldsymbol{x}_i)\, \boldsymbol{p}(\boldsymbol{x}_i)\, \boldsymbol{p}^T(\boldsymbol{x}_i), \tag{38}$$

where n is the number of nodes in the neighborhood of point $\boldsymbol{x}$ where the weight function $w(\boldsymbol{x} - \boldsymbol{x}_i) \neq 0$. The commonly used

cubic spline weight function is used here:

$$w(r) = \begin{cases} \frac{2}{3} - 4r_s^2 + 4r_s^3 & r_s \leq \frac{1}{2} \\[2mm] \frac{4}{3} - 4r_s + 4r_s^2 - \frac{4}{3}r_s^3 & \frac{1}{2} < r_s \leq 1 \ , \\[2mm] 0 & r_s > 1 \end{cases} \tag{39}$$

where r_s is the radius of the support domain for node i.

An efficient extrinsic enrichment, similar to XFEM, is adopted to account for discontinuities or singularities within the support domain. The extrinsically enriched displacement approximation for a typical point $\boldsymbol{x}$ can be written as [43, 44]:

$$\boldsymbol{u}^h(\boldsymbol{x}) = \sum_{i=1}^{n} \phi_i(\mathbf{x})\, \boldsymbol{u}_i + \sum_{k=1}^{m_t} \phi_k \sum_{\alpha=1}^{4} Q_\alpha(\mathbf{x})\, \boldsymbol{b}_k, \tag{40}$$

where $\boldsymbol{b}_k$ is the vector of additional degrees of freedom for modeling crack tips, m_t is the set of nodes that the discontinuity is in its influence (support) domain, and $Q_\alpha(\mathbf{x})$ are the enrichment functions. The first term in the right-hand side of Eq. (40)

Table 3. Average and maximum errors of SIFs (mode I) for different J-integral domains.

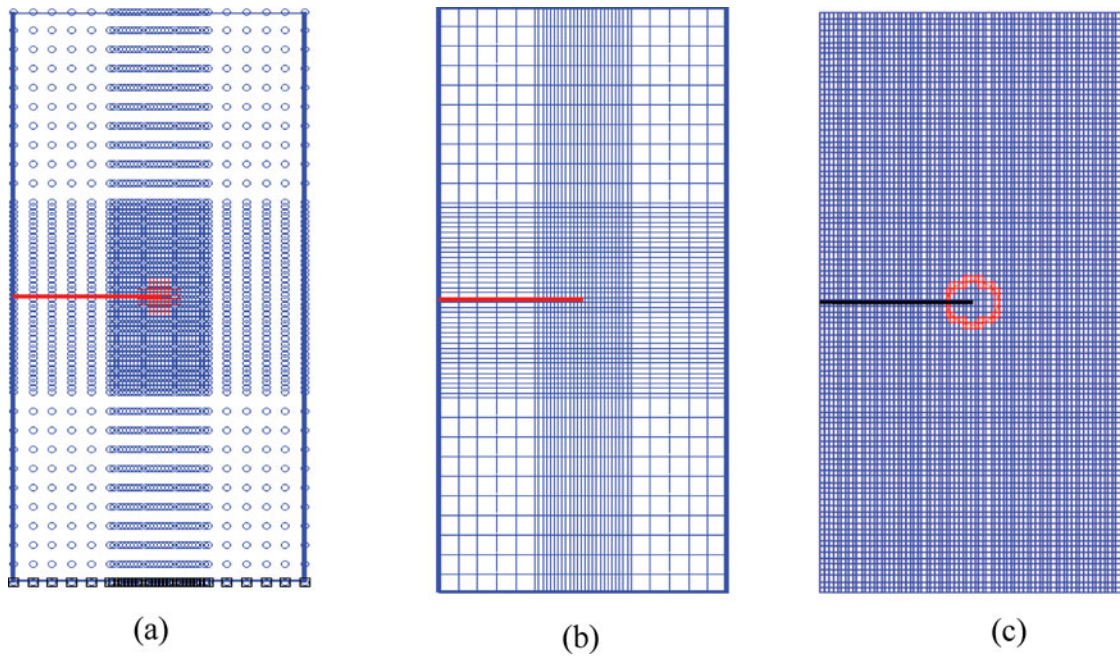| Error %	d_{max}		
	1.7	2	2.3
Average	0.26	3.97	13.91
Maximum	0.71	9.11	23.24

Figure 13. (a) Nodal distribution, (b) adaptive background cells, and (c) uniform background cells used for modeling of the rectangular functionally graded plate.

is the classical EFG approximation to determine the displacement field, while the second term is the enrichment approximation in order to accurately represent the analytical solution near the crack tip.

The orthotropic enrichment functions (that will be used in Eq. (40)) are used extrinsically for anisotropic materials to enrich the MLS formulation [36]:

$$Q(r, \theta) = \left(\sqrt{r} \cos\left(\frac{\theta_1}{2}\right) \sqrt{g_1(\theta)}, \sqrt{r} \cos\left(\frac{\theta_2}{2}\right) \sqrt{g_2(\theta)}, \right.$$
$$\left. \times \sqrt{r} \sin\left(\frac{\theta_1}{2}\right) \sqrt{g_1(\theta)}, \sqrt{r} \sin\left(\frac{\theta_2}{2}\right) \sqrt{g_2(\theta)} \right),$$
$$(41)$$

where

$$\theta_j = \arctan\left(\frac{s_{jy} \sin(\theta)}{\cos(\theta) + s_{jx} \sin(\theta)}\right) (j = 1, 2), \quad (42)$$
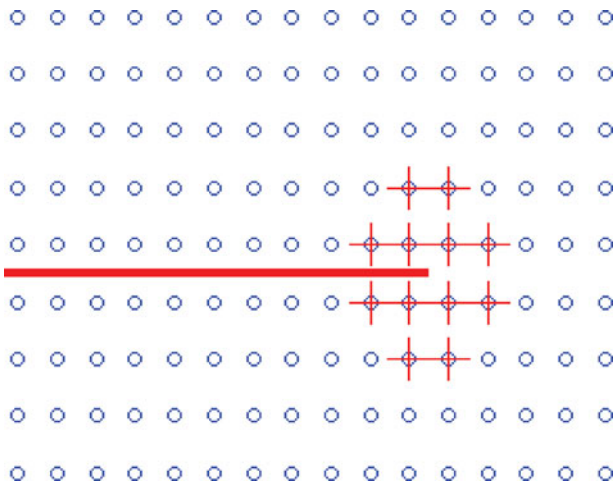

Figure 14. Enrichment nodes around the crack tip.

$$g_j(\theta) = \sqrt{(\cos(\theta) + s_{jx}\sin(\theta))^2 + (s_{jy}\sin(\theta))^2}, \quad (43)$$

where $s_j = s_{jx} + i s_{jy}$ are the roots of the characteristic equation (6).

Discretization of Eq. (35) results in:

$$\begin{bmatrix} K & Q \\ Q^T & 0 \end{bmatrix} \begin{bmatrix} U \\ \lambda \end{bmatrix} = \begin{bmatrix} F \\ q \end{bmatrix}, \quad (44)$$

where K is the global stiffness matrix, F is the global force vector, Q and q are the Lagrange related terms for enforcement of the boundary conditions by the Lagrange multipliers λ:

$$Q = -\int_{\Gamma_u} N^T \phi d\Gamma, \quad (45)$$

$$q = -\int_{\Gamma_u} N^T \bar{u} d\Gamma, \quad (46)$$

$$\lambda(\mathbf{x}) = \sum_{i=1}^{n_\lambda} N_i(\mathbf{x}) \lambda_i, \quad (47)$$

where N stands for Lagrange interpolation shape functions over the boundary Γ_u with n_λ nodes.

Table 4. Comparison of normalized SIFs for different background cells for the edge-cracked plate subjected to shear load ($r_J = 0.6$, $d_{max} = 2.3$).

	K_I			K_{II}		
E_2/E_1	Ref. [3]	XEFGM31 × 33	XEFGM35 × 59	Ref. [3]	XEFGM31 × 33	XEFGM35 × 59
0.5	1.110	1.094	1.102	1.093	1.034	1.080
0.556	1.092	1.077	1.083	1.078	1.022	1.064
0.667	1.061	1.047	1.055	1.052	1	1.042
0.833	1.016	1.012	1.018	1.014	0.974	1.012
1	0.996	0.985	0.997	0.997	0.953	0.989
1.25	0.962	0.952	0.966	0.967	0.923	0.957
2	0.893	0.887	0.891	0.905	0.876	0.905
2.5	0.862	0.858	0.861	0.877	0.852	0.877
5	0.772	0.773	0.774	0.791	0.779	0.798
10	0.689	0.695	0.696	0.708	0.707	0.721

Note: The values have been normalized by the exact solution for a uniform E.
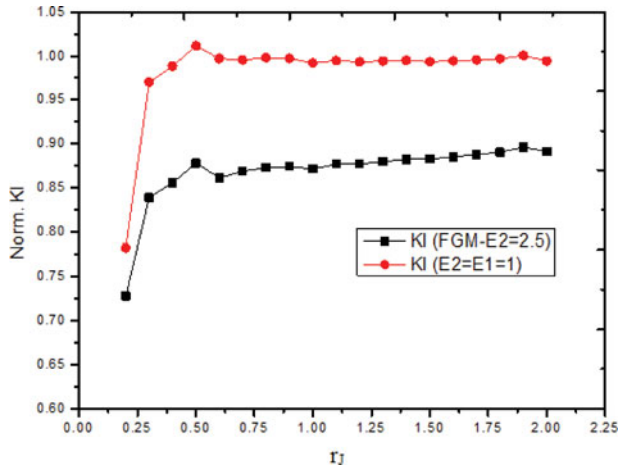
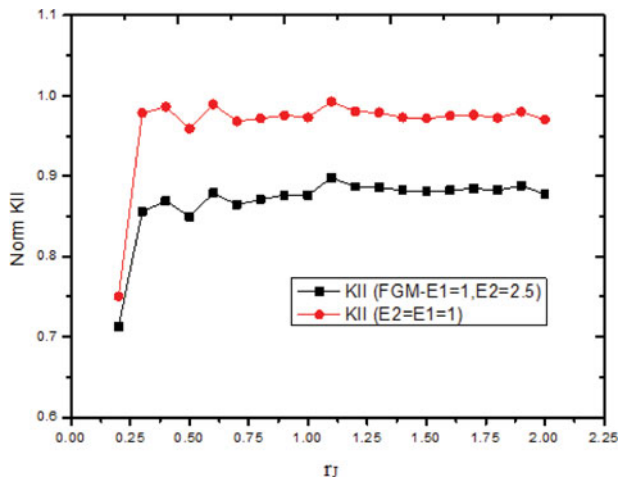**Figure 15.** Values of K_I for various relative r_J.

Figure 16. Values of SIF K_{II} for various relative r_J.

Table 5. Error of normalized stress intensity factor (mode I) for different background cells.

Uniform background cells	Area of crack tip cell	Error of K_I (%)	Error of K_{II} (%)
39 × 59	0.0486	8.00	4.79
49 × 69	0.0331	1.97	3.76
75 × 99	0.0150	0.69	2.50

K and F are assembled from the nodal stiffness matrix and nodal force vector, respectively:

$$K_{ij}^n = \begin{bmatrix} K_{ij}^{uu} & K_{ij}^{ub} \\ K_{ij}^{bu} & K_{ij}^{bb} \end{bmatrix}, \tag{49}$$

$$F_i^n = \left\{ F_i^u \ F_i^{b_1} \ F_i^{b_2} \ F_i^{b_3} \ F_i^{b_4} \right\}^T, \tag{50}$$

where

$$K_{ij}^{rs} = \int_\Omega \left(B_i^r \right)^T D B_j^s d\Omega \quad (r, s = u, b), \tag{51}$$

$$F_i^u = \int_\Omega \phi_i^t b d\Omega + \int_{\Gamma_t} \phi_i^T \bar{t} d\Gamma, \tag{52}$$

$$F_i^{b_a} = \int_\Omega \phi_i^T Q_a b d\Omega + \int_{\Gamma_t} \phi_i^T Q_a \bar{t} d\Gamma \quad (a = 1, 2, 3, 4) \tag{53}$$

B_i^u and B_i^b are matrices of shape function derivatives:

$$B_i^u = \begin{bmatrix} \phi_{i,x} & 0 \\ 0 & \phi_{i,y} \\ \phi_{i,y} & \phi_{i,x} \end{bmatrix}, \tag{54}$$

$$B_i^b = \left[B_i^{b_1} \ B_i^{b_2} \ B_i^{b_3} \ B_i^{b_4} \right], \tag{55}$$

$$B_i^u = \begin{bmatrix} (\phi_i Q_\alpha)_{,x} & 0 \\ 0 & (\phi_i Q_\alpha)_{,y} \\ (\phi_i Q_\alpha)_{,y} & (\phi_i Q_\alpha)_{,x} \end{bmatrix} \quad (\alpha = 1, 2, 3, 4). \tag{56}$$

U is the global displacement vector that collects the displacements of all nodes in the entire problem domain and additional enrichment degrees of freedom:

Strain and stress components can then be retrieved from nodal displacements u^h using Eqs. (57) and (58), respectively:

$$U = \left\{ u \ b_1 \ b_2 \ b_3 \ b_4 \right\}^T. \tag{48}$$

$$\varepsilon = L u^h, \tag{57}$$

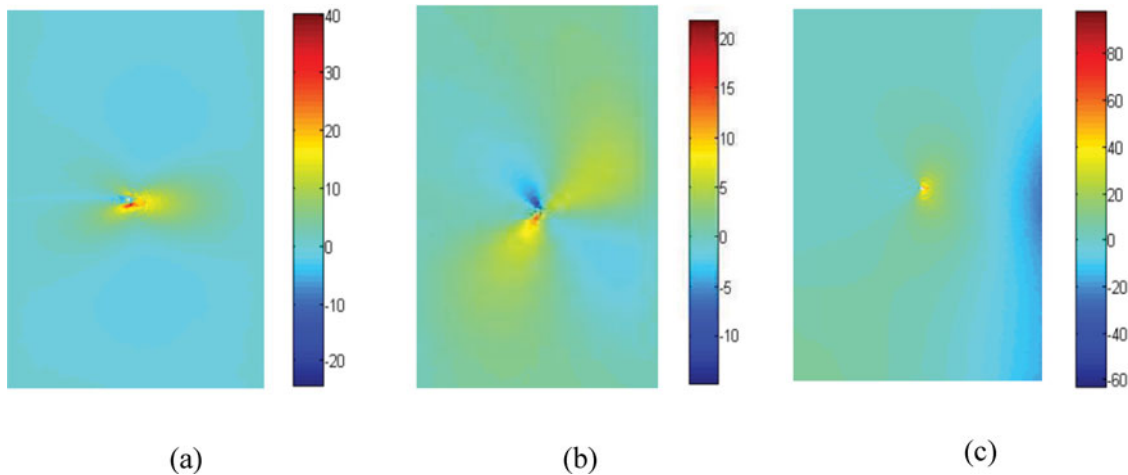$$\sigma = D\varepsilon. \tag{58}$$

(a)   (b)   (c)

Figure 17. Zoom contours of stresses of the edge crack FGM plate under shear loading ($E_2/E_1 = 2.5, r_J = 0.6, d_{max} = 2.3$, 2256 field nodes, 13 gauss points for each sub-triangle). Units of stress are MPa.

5.1. *Appropriate domain of influence*

There are several methods available in the literature to introduce discontinuities in meshless methods. They differ on the way they represent the displacement approximation of a point on a specific side of the crack from the displacement field of the nodes on the opposite side of the crack. Among them, the visibility criterion and the diffraction method have been frequently used in EFG fracture analysis. In the visibility method, the crack boundary is considered to be opaque, and any nodes on the opposite side of the crack are excluded from the support domain of a node for approximating the displacement field. Difficulties arise for particles close to the crack tip since undesired interior discontinuities occur [27]. On the other hand, the diffraction method is motivated by the way light diffracts around a sharp corner.

In the present article, appropriate selection for the support domain near a crack tip is based on a similar approach adopted by [25], as depicted in Figure 4. For each point $\mathbf{x_1}$, the nodes on the opposite side of the crack face are not considered. In order to take into account the effect of discontinuity near a crack tip $\mathbf{x_c}$, indirect distance of $s_1 + s_2(\mathbf{x})$ is considered instead of the direct distance of $s_0(\mathbf{x})$, as shown in Figure 4b:

$$\begin{cases} s_0\left(\mathbf{x}\right) = \mathbf{x} - \mathbf{x_1} \\ s_1\left(\mathbf{x}\right) = \mathbf{x_1} - \mathbf{x_c} \\ s_2\left(\mathbf{x}\right) = \mathbf{x} - \mathbf{x_c} \end{cases} . \tag{59}$$

5.2. *Numerical integration by the sub-triangle technique*

Usually the Gauss quadrature rule is employed for numerical integration inside the background cell of the EFG mesh-free method. Existence of a discontinuity within a background cell may result in substantial accuracy reduction. Many researchers demonstrated that a regular increase in the order of Gauss integration does not necessarily improve the accuracy of integration
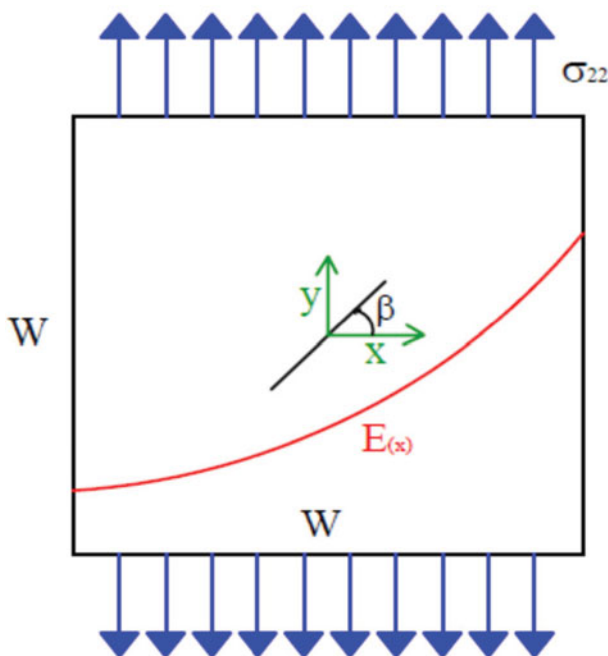
Figure 18. FGM plate with an interior crack under mixed-mode loading.

over a discontinuous element/cell, whereas independent integration of each side of the discontinuity with even low-order rules does guarantee an accurate integration [25]. Thus, an efficient technique is required to define the necessary points needed for the integration within these background cells, while remaining consistent with the crack geometry.

An approach similar to the one proposed by [45] and originally utilized by [25] is adopted. Any background cell that intersects with a crack is subdivided at both sides into sub-triangles whose edges are adapted to the crack faces, as illustrated in Figure 5. It is important to note that, while triangulation of the crack tip element substantially improves the accuracy of integration by increasing the order of Gauss quadrature, it also avoids numerical complications of singular fields at the crack tip because none of the Gauss points are placed on the position of the crack tip.

6. Numerical case studies

Several case studies are presented in this section to illustrate the application of EFG mesh-free method for crack analysis of FGMs. In addition, the sub-triangular technique near the crack tip, appropriate support domain in the location of the crack and crack tip, the proper nodal distribution for local crack region and for the whole geometry, and the interaction integral method with the incompatibility formulation are adopted to calculate SIFs for cracked FGMs.

6.1. *Edge cracked FGM plate under tension*

In this problem, an edge crack parallel to the material gradation in a rectangular FGM plate is considered. The plate is subjected to a uniform tensile loading, as depicted in Figure 6.

The geometry of the cracked plate is described by: width $b = 10$ mm, length $2h = 30$ mm, and crack length $a = 0.4b$. The material gradation in the x_1-direction parallel to the crack is described by an exponential law:

$$E\left(x_1\right) = E o e^{\alpha x_1}, \alpha = \frac{1}{b} \ln\left(\frac{Ew}{Eo}\right), \tag{60}$$

where $E_0 = 10,000$ MPa and $E_w = 50,000$ MPa are the Young's modulus at the left and right side of the plate, respectively. The Poisson's ratio is taken as $v = 0.25$ and the plane strain condition is assumed in the numerical calculations.

Also, a linear basis function $\boldsymbol{p}^T(x) = [1\ x\ y]$ and the cubic spline weight function with circular support domain ($r = 1.7$) are selected. Integration of each sub-triangle cell is performed by 13 Gauss points near the crack tip.

Further, 376 nonuniformly distributed nodes are used to simulate the model. Numerical integration is performed on a background mesh of 682 cells with a 2×2 Gauss quadrature rule in each cell. The background cells and nodal distribution are depicted in Figure 7.

Gauss points distribution around the crack using the typical and sub-triangles techniques are shown in Figure 8. The cell that includes a crack tip is divided into six sub-triangles, whereas the cell that cuts a crack edge is divided into four sub-triangles.
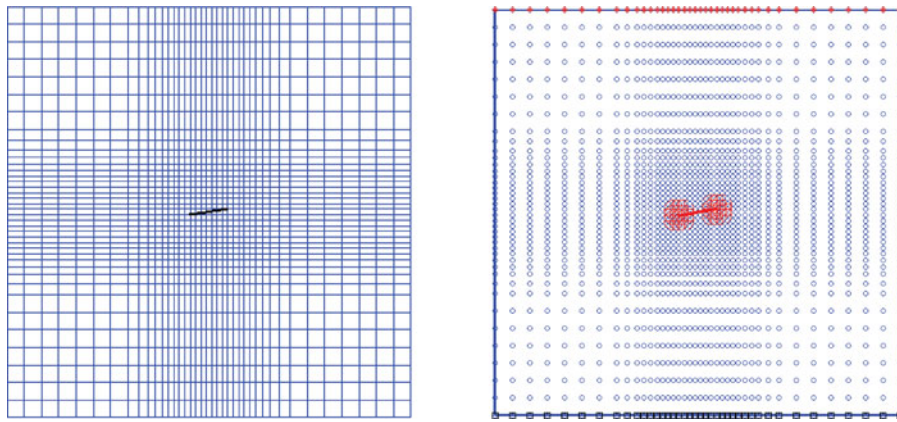
Figure 19. Background cells and nodal distribution used for modeling the FGM plate with a central crack ($\beta = 10$).
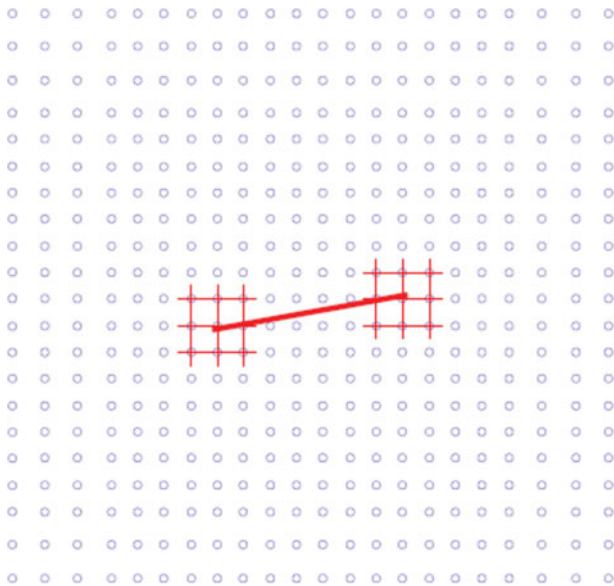

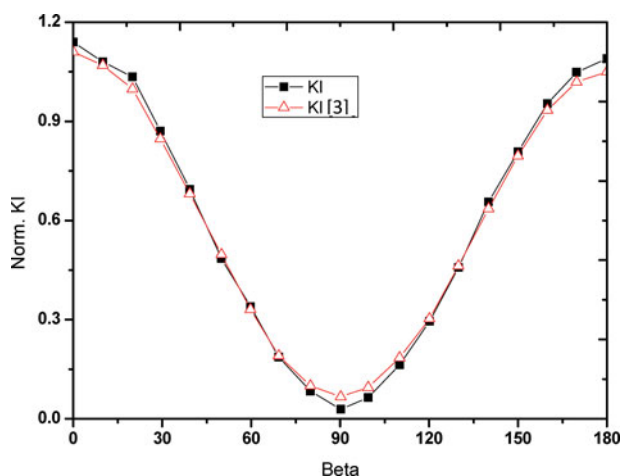**Figure 20.** Enrichment nodes around the crack tip.

Figure 21. Normalized mode I stress intensity factor for the inclined center crack.

Table 1 compares the results of the proposed method with [9], which used the boundary element method based on a boundary-domain integral formulation, consisting of 431 nodes for the half model. Better results are obtained with $r_J = 0.6$ (r_J is the radius of the J integral).

It can be observed that the error of the normalized SIF of the ordinary technique in comparison with the reference value for the homogenous case is about 9.5% (at $E_1 = E_2$, $r_J = 0.5$). This shows the inefficiency of the ordinary technique to capture the correct SIF of the FGM plate with the same number of nodes as used for the sub-triangle technique.

To further clarify the effect of nonuniform background cells on the solution accuracy, four nonuniform background cells have been selected, as shown in Figure 9. Figure 9 clearly shows that when the number of cells is increased, better results are obtained. The number of nodes with the enrichment functions must be sufficient to obtain sufficiently accurate results especially for complicated problems, such as the edge crack plate under shear loading.

Optimal background mesh has to be selected to avoid unnecessary computational costs while providing the required accuracy. Figure 9 illustrates the result of a number of background cells with and without the sub-triangular technique, in comparison with the reference values.

Similar comparisons are made for the finest background cells, as shown in Figure 10. In any case (homogenous material or FGM), the results of the proposed method remain accurate for a wide range of r_J values, as clearly seen from Figure 11. As a result, the size of the J-integral domain (r_J) does not substantially affect the values of SIFs. Also, Table 2 shows that by the increase of the
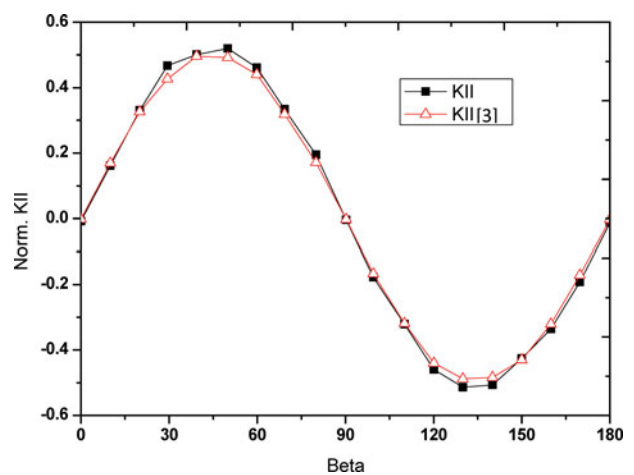

Figure 22. Normalized mode II stress intensity factor for the inclined center crack.

Table 6. Normalized SIFs for $d_{max} = 1.7$, 1672 field nodes, 13 Gauss points for each sub-triangle.

	($\beta = 10°$)		($\beta = 50°$)		($\beta = 80°$)		($\beta = 120°$)		($\beta = 160°$)	
r_J	K_I (1.070)*	K_{II} (0.169)*	K_I (0.497)*	K_{II} (0.492)*	K_I (0.100)*	K_{II} (0.173)*	K_I (0.303)*	K_{II} (−0.440)*	K_I (0.934)*	K_{II} (−0.321)*
0.3	1.080	0.162	0.485	0.520	0.095	0.181	0.295	−0.456	0.954	−0.336
0.4	1.121	0.180	0.531	0.522	0.090	0.183	0.294	−0.459	0.984	−0.338
0.5	1.163	0.189	0.533	0.537	0.081	0.194	0.288	−0.464	0.980	−0.350
0.6	1.186	0.201	0.531	0.545	0.074	0.199	0.294	−0.462	0.974	−0.356
0.7	1.179	0.210	0.530	0.549	0.073	0.199	0.291	−0.469	0.966	−0.357

Note: ()* are the reference values.

number of Gauss points in each sub-triangle, the error of SIFs decreases.

Despite exponential grading in material property, as depicted in Figure 12, very smooth stress contours are obtained without any additional treatment, as it is necessary in conventional FEM through the stress extrapolation or stress recovery techniques.

Figure 12d illustrates the inefficiency of conventional mesh-less method without enrichment functions in capturing the stress singularity at the crack tip, compared with the singular stress contour previously depicted in Figure 12c. The normalized SIF of un-enriched solution is 1.662, compared with the reference value of 1.741 [9].

It is also clearly observed that the right edge bears higher σ_{yy} stress, because of higher stiffness, when E_2/E_1 becomes more than 25. In addition, by the proposed method, the ratio of the elapsed time for solving the problem with appropriate support domain to the typical support domain in the vicinity of the crack is equal to 0.78 (2.91% error of mode I SIF) for $\alpha b = 0.339$, and 13 Gauss points in each sub-triangle.

Finally, Table 3 illustrates the effect of size of support domain on the accuracy of mode I SIF for different J-integral domains. The best results are obtained for size of support domain $d_{max} = 1.7$ mm. The average value is computed from the average error of all SIFs for different J-integral domains (but for a certain size of the support domain, d_{max}). The maximum valve represents the largest error of SIFs for different J-integral domains (for a certain size of the support domain, d_{max}).

6.2. Edge crack FGM plate with shear loading

In order to demonstrate the capabilities of the proposed mesh-less approach for a general case of mixed-mode fracture, an edge-cracked plate subjected to a shear load is considered. The problem geometry is shown in Figure 6 ($2h = 16$ mm, $b = 7$ mm, $a = 3.5$ mm), where the bottom edge is clamped and the top edge is subjected to a shear load.

The Young's modulus is taken to be variable with position, as given by Eq. (60). A set of 2256 nonuniformly distribution nodes

Table 7. Normalized SIFs vs. d_{max} ($\beta = 120°$, 1672 field nodes, and 13 gauss points for each sub-triangle).

	$d_{max} = 1.7$		$d_{max} = 2.0$		$d_{max} = 2.3$	
r_J	K_I	K_{II}	K_I	K_{II}	K_I	K_{II}
0.3	0.295	−0.456	0.275	−0.442	0.270	−0.465
0.4	0.294	−0.459	0.285	−0.464	0.284	−0.483
0.5	0.288	−0.464	0.299	−0.478	0.303	−0.491
0.6	0.294	−0.462	0.304	−0.482	0.316	−0.496
0.7	0.291	−0.469	0.306	−0.473	0.325	−0.490

and a 35×59 background mesh are used for simulation of the problem, as depicted in Figure 13. The results of this section have been obtained using a circular domain of influence and the size of the support domain is considered as $d_{max} = 2.3$ mm. Thus, 12 nodes around the crack tip are selected for enrichment of the solution, as shown in Figure 14.

Dolbow and Gosz [3] solved this problem by using the extended finite element method on a uniform mesh of 48×96
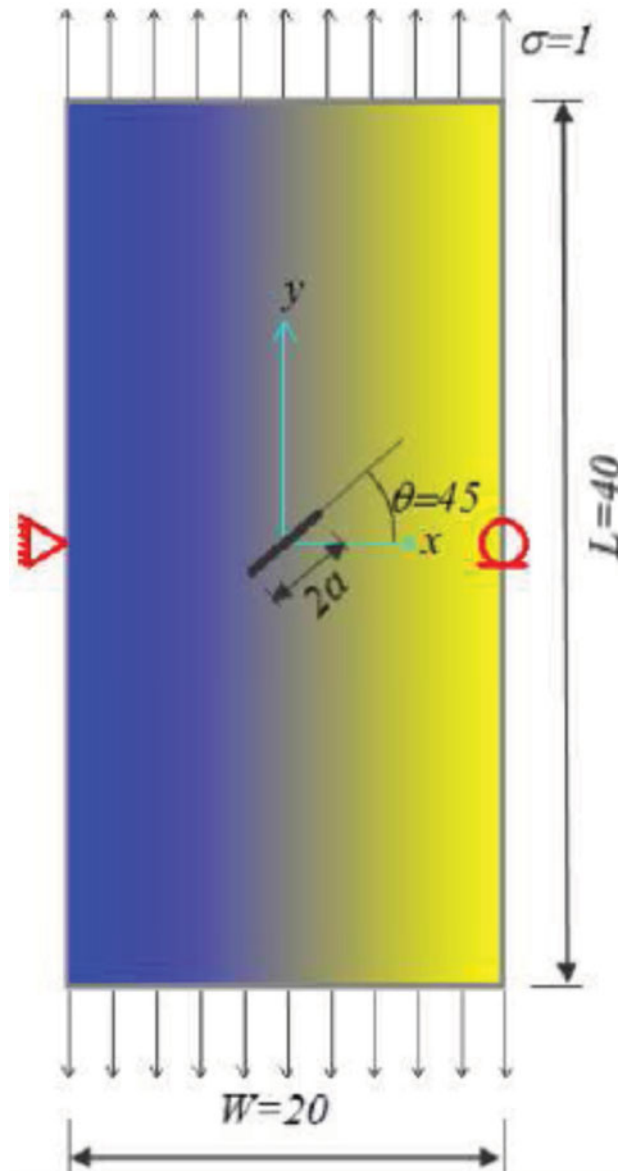
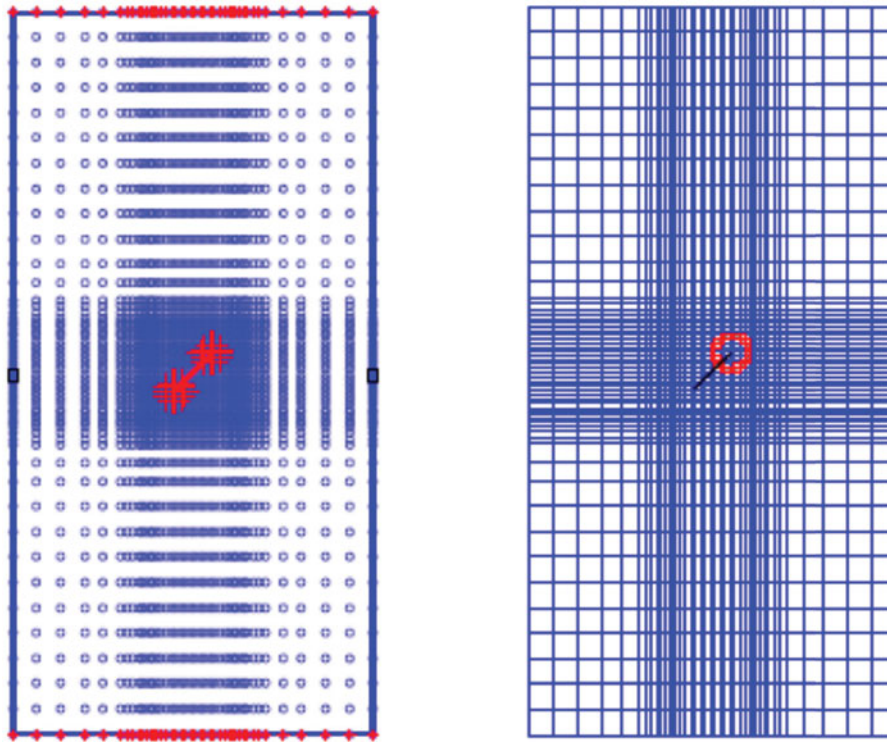**Figure 23.** Orthotropic FGM rectangular plate with an inclined crack.

Figure 24. Distribution of nodes and background cells.

quadrilateral elements to extract the final results. Table 4 illustrates that the results of the proposed method with 35×59 background cells are close to the results of [3], while using approximately half number of nodes. Table 4 also demonstrates that for the case of 31×33 background cells, a good convergence is obtained for K_I [3], but the results for K_{II} [3] are relatively poor. Therefore, optimum background cell numbers are required to reduce the time cost while achieving the necessary accuracy for this mixed mode problem.

As an additional check, a sensitivity analysis is performed with respect to the size of the J-integral, as depicted in Figures 15 and 16.

The corresponding contours of stresses are depicted in Figure 17. As in the previous two cases, the proposed method with appropriate support domain in the vicinity of crack has reduced the time cost, and the error. For example, the ratio of the elapsed time for solving the problem with appropriate support domain to ordinary support domain near the crack is equal
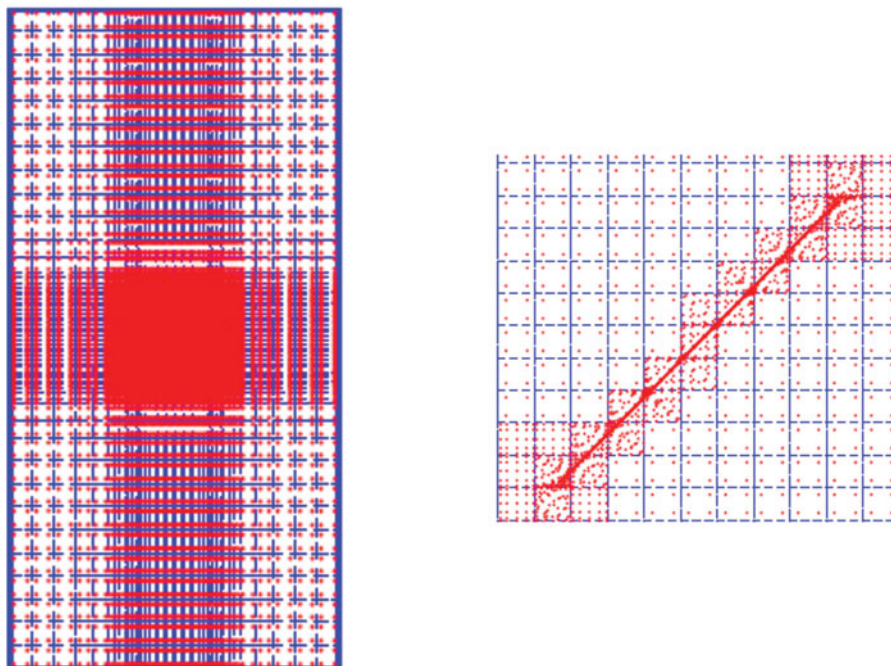

Figure 25. Distribution of Gauss point and the background cells around the crack tip.

Table 8. Stress intensity factors for mixed mode crack in a rectangular plate ($r_J/a = 0.5$, $d_{max} = 1.7$).

Material properties			SIFs		
α	β	γ	K_I	K_{II}	Reference
0	0	0	1.0611	1.0256	Present XEFGM
0	0	0	1.0670	1.0440	Kim and Paulino (MCC) [40]
0	0	0	1.0770	1.0350	Kim and Paulino (DCT) [40]
0.2	0.2	0.2	1.8267	1.4601	Present XEFGM
0.2	0.2	0.2	1.7620	1.4390	Kim and Paulino (MCC) [40]
0.2	0.2	0.2	1.7690	1.4190	Kim and Paulino (DCT) [40]
0.2	0.2	0.2	1.4075	1.1723	Bayesteh and Mohammadi [17]
0.5	0.4	0.3	2.2521	1.5716	Present XEFGM
0.5	0.4	0.3	2.3840	1.5810	Kim and Paulino (MCC) [40]
0.5	0.4	0.3	2.3870	1.5530	Kim and Paulino (DCT) [40]
0.5	0.4	0.3	2.3554	1.4482	Bayesteh and Mohammadi [17]

to 0.61 (6.94 and 7.95% are the errors of mode I and II SIFs, respectively) for the input data of Table 4 at $E_2/E_1 = 2$ and 35×59 background cells.

In addition, uniform background cells (schematically depicted in Figure 13c for 75×99 cells) are used to study the effect of the number of cells on the value of mode I SIF, as demonstrated in Table 5 where 39×59, 49×69, and 75×99 background cells have been analyzed based on the sub-triangle technique at $E_2 = 2.5$, $r_J = 0.6$, $d_{max} = 2.3$, and 2256 field nodes.

6.3. FGM plate with inclined center crack

Consider a centrally located inclined crack of length $2a = 2$ units and an orientation β in a finite 2D square plate of size $W \times W$ ($W = 20$ units), as shown in Figure 18. Plane stress conditions are assumed with a constant Poisson's ratio of $\nu = 0.3$. The plate is subjected to a uniform far-field state of stress σ_{yy}. The elastic modulus is assumed to be an exponential function, given by Eq. (60).

The meshless discretization involves a total of 1672 nodes and 39×39 background cells. Integration of each sub-triangle cell is performed by 13 Gauss points near the crack tip ($r_J = 0.3$) and for other cells, a 2×2 Gauss quadrature rule is used.

The domain of influence is circular and the size of the support domain is considered to be 1.7. Nine nodes (providing an extra 72 degrees of freedom) around each crack tip are selected for enrichment, as typically shown in Figures 19 and 20. The results for K_I as a function of β are reported for $\alpha = 0.1$ in Figure 21. Also, analogous results for K_{II} are shown in Figure 22. In both plots, results are reported for the rightmost crack tip when $\beta = 0$. Consequently, Dolbow and Gosz [3] used XFEM with 60×60 quadrilateral elements to solve the same problem.

As in previous cases, proper background cells must be selected to capture the reference values and to save the time. In this example, accurate SIFs are obtained when the range of relative r_J is bounded between 0.3 to 0.4 (see Table 6). Finally, Table 7

Table 9. The effect of the number of the nodes on SIFs, $\alpha = \beta = \gamma = 0.2$ ($r_J/a = 0.5$, $d_{max} = 1.7$).

No. of nodes (nnx × nny)	K_I ([40] = 1.769)	K_{II} ([40] = 1.419)
2516 (40 × 56 bk cell)	1.8267	1.4601
3156 (48 × 60 bk cell)	1.8401	1.5761
4160 (54 × 66 bk cell)	1.7235	1.4346
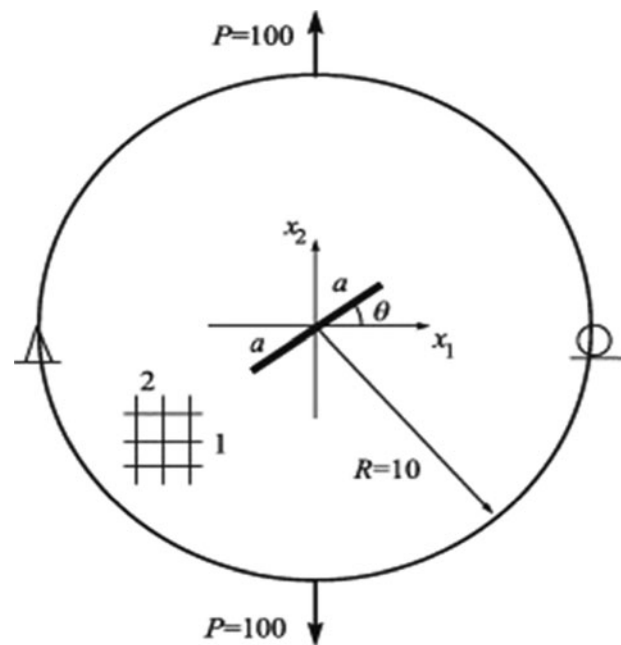
Figure 26. Geometry and boundary conditions for an orthotropic disk with inclined central crack subjected to point loads.

presents the insensitivity of the results of SIFs of the mixed mode problem in comparison with the change in the values of r_J and d_{max}.

6.4. Orthotropic FGM rectangular plate with an inclined crack (nonproportional distribution)

An orthotropic FGM rectangular plate with an inclined crack is considered, as depicted in Figure 23. This problem has already been investigated by several researchers, such as in [38] for homogeneous orthotropic case (no variation in material properties), and by [17] and [40] for various orthotropic FGM cases. In [40] the finite element method and the modified crack closure approach were used, while XFEM was used in [17]. Functions of material properties distribution follow the exponential form:

$$E_{11}(x) = E_{11}^O e^{\alpha x}, \ E_{22}(x) = E_{22}^O e^{\beta x}, \ G_{12}(x) = G_{12}^O e^{\gamma x}, \quad (61)$$

where α, β, and γ are the material nonhomogeneity parameters for gradation of E_{11}, E_{22}, and G_{12}, respectively.

Material and geometric properties are:

$$2a = 2\sqrt{2}, \frac{L}{w} = 2,$$
$$E_{11}^O = 3.5 \times 10^6 \text{MPa}, E_{22}^O = 12 \times 10^6 \text{MPa},$$
$$G_{12}^O = 3 \times 10^6 \text{MPa}, \upsilon_{12} = 0.204.$$

In this case, 2516 nodes and 40×56 background cells are used to model the specimen, as shown in Figures 24 and 25, whereas 3694 nodes were used in [40]. The EFG is adopted for the first time for orthotropic FGMs, along with the enrichment functions (54).

Almost identical results are obtained, as compared in Table 8 for different cases. It is observed from Table 8 that the results of the present work are close to the results of [40] for all different material properties. This demonstrates the efficiency of the extended EFGM for fracture analysis of complicated problems.
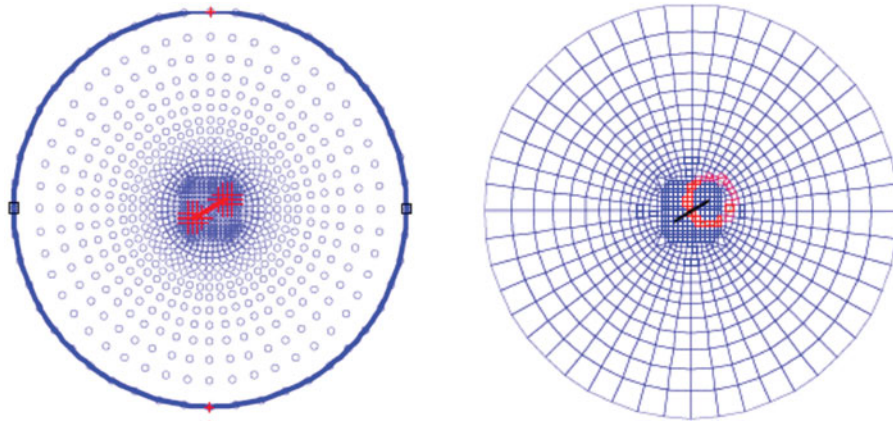
Figure 27. Distribution of nodes and background cells.

The effect of the number of nodes on SIF values at $\alpha = \beta = \gamma = 0.2$ is shown in Table 9. Clearly, when the number of the nodes increases, the error of the solution decreases.

Table 10. SIFs for an inclined center crack in a circular disk considering radial gradation $\beta a = \alpha a = \gamma a$, $d_{max} = 1.7$, $r_J = 1.6/a$.

βa	K_I	K_{II}	K_I [46]	K_{II} [46]	K_I [36]	K_{II} [36]
−0.5	28.58	19.12	29.22	18.56	—	—
−0.25	23.13	16.51	23.16	15.21	—	—
0.0	17.11	12.11	16.73	11.33	17.08	11.65
0.25	10.87	7.41	10.57	7.318	—	—
0.5	5.76	3.75	5.459	3.847	—	—

Table 11. SIFs for an inclined center crack in a circular disk considering radial gradation, $d_{max} = 1.7$, $r_J = 1.6/a$.

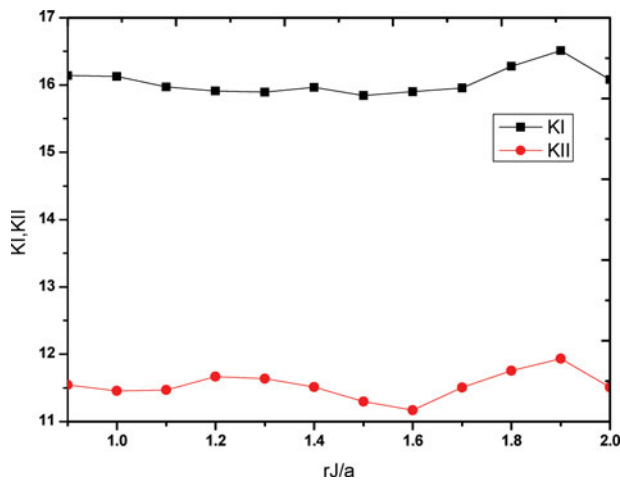| Case	Non-homogeneity parameters	K_I	K_{II}	K_I [46]	K_{II} [46]
1	$\alpha a = 0.1$, $\beta a = 0.0$, $\gamma a = 0.0$	15.25	11.05	15.45	10.42
2	$\alpha a = 0.0$, $\beta a = 0.1$, $\gamma a = 0.0$	17.87	12.05	17.08	11.50
3	$\alpha a = 0.0$, $\beta a = 0.0$, $\gamma a = 0.1$	15.90	11.16	16.73	11.33

Figure 28. SIFs vs. r_J/a.

6.5. *Orthotropic FGM disk with an inclined center crack*

The problem, depicted in Figure 26, shows a circular disk with a center crack inclined by $\theta = 30°$. A point load is applied on the top and bottom nodes, i.e., $P = \pm 100$. The displacement boundary conditions are prescribed such that $(u_1, u_2) = (0, 0)$ for the node at $(x_1, x_2) = (-10, 0)$ and $u_2 = 0$ for the node at $(x_1, x_2) = (10, 0)$. Exponential material gradations with respect to the radial (r) are considered as:

$$E_{11}(r) = E_{11}^O e^{\alpha r}, \ E_{22}(r) = E_{22}^O e^{\beta r}, \ G_{12}(r) = G_{12}^O e^{\gamma r}, \quad (62)$$

$$r = \sqrt{x_1^2 + x_2^2}, \quad (63)$$

and

$$E_{11}^O = 0.1, \ E_{22}^O = 1.0, \ G_{12}^O = 0.5, \ \upsilon_{12} = 0.03.$$

The mesh discretization consists of 957 nodes, as depicted in Figure 27.

Table 10 shows the results of SIFs for the isotropic and orthotropic cases considering various material nonhomogeneity parameter βa. Table 11 compares similar results for different nonhomogeneity variations. Variation of SIFs with respect to values of r_J/a for the case number 3 from Table 11 is depicted in Figure 28. Clearly, no sensitivity is observed.

7. Conclusion

Development of the XEFGM method for isotropic and anisotropic FGMs crack analysis along with the use of the sub-triangle technique for numerical integration, appropriate support domain, and the enrichment functions in the crack location has significantly increased the accuracy of the solution. The triangulation technique substantially improves the accuracy of integration by increasing the order of Gauss quadrature, and avoids numerical complications of singular fields at the crack tip because none of the Gauss points are placed on the position of the crack tip. The use of the incompatible interaction integral method provides very accurate results for the values of SIFs in mixed mode fracture analysis of FGMs.

Acknowledgment

References

[1] I. Shiota and Y. Miyamoto, Functionally graded materials, Proceedings of the 4th International Symposium on Functionally Graded Materials, October 21–24, Tsukuba, Japan, 1996.

[2] F. Delale and F. Erdogan, The crack problem for a non-homogeneous plate, J. Appl. Mech., vol. 50, no. 3, pp. 609–614, 1983.

[3] J.E. Dolbow and M. Gosz, On the computation of mixed-mode stress intensity factors in functionally graded materials, Int. J. Solids Struct., vol. 39, pp. 2557–2574, 2002.

[4] B.N. Rao and S. Rahman, Mesh-free analysis of cracks in isotropic functionally graded materials, Eng. Fract. Mech., vol. 70, pp. 1–27, 2003.

[5] J.-H. Kim and G. H. Paulino, An accurate scheme for mixed-mode fracture analysis of functionally graded materials using the interaction integral and micromechanics models, Int. J. Numer. Methods Eng., vol. 58, pp. 1457–1497, 2003.

[6] J.-H. Kim and G.H. Paulino, Consistent formulations of the interaction integral method for fracture of functionally graded materials, J. Appl. Mech., vol. 72, pp. 351–364, 2005.

[7] K.Y. Dai, G.R. Liu, K.M. Lim, X. Han, and S.Y. Du, A meshfree radial point interpolation method for analysis of functionally graded material (FGM) plates, Comput. Mech., vol. 34, pp. 213–223, 2004.

[8] J. Sladek, V. Sladek, and C. Zhang, A meshless local boundary integral equation method for dynamic anti-plane shear crack problem in functionally graded materials, Eng. Anal. Bound. Elem., vol. 29, pp. 334–342, 2005.

[9] X.W. Gao, Ch. Zhang, J. Sladek, and V. Sladek, Fracture analysis of functionally graded materials by a BEM, Compos. Sci. Technol., vol. 68, pp. 1209–1215, 2008.

[10] A. Asadpoure, S. Mohammadi, and A. Vafai, Modeling crack in orthotropic media using a coupled finite element and partition of unity methods, Finite Elem. Anal. Des., vol. 42, pp. 1165–1175, 2006.

[11] A. Asadpoure, S. Mohammadi, and A. Vafai, Crack analysis in orthotropic media using the extended finite element method, Thin-Walled Struct., vol. 44, pp. 1031–1038, 2006.

[12] D. Motamedi and S. Mohammadi, Dynamic analysis of fixed cracks in composites by the extended finite element method, Eng. Fract. Mech., vol. 77, pp. 3373–3393, 2010.

[13] D. Motamedi and S. Mohammadi, Dynamic crack propagation analysis of orthotropic media by the extended finite element method, Int. J. Fract., vol. 161, pp. 21–39, 2010.

[14] D. Motamedi and S. Mohammadi, Fracture analysis of composites by time independent moving-crack orthotropic XFEM, Int. J. Mech. Sci., vol. 54, pp. 20–37, 2012.

[15] S. Esna Ashari and S. Mohammadi, Delamination analysis of composites by new orthotropic biomaterial extended finite element method, Int. J. Numer. Methods Eng., vol. 86, no. 13, pp. 1507–1543, 2011.

[16] S.S. Ghorashi, N. Valizadeh, and S. Mohammadi, Extended isogeometric analysis for simulation of stationary and propagating cracks, Int. J. Numer. Methods Eng., vol. 89, no. 9, pp. 1069–1101, 2011.

[17] H. Bayesteh and S. Mohammadi, XFEM fracture analysis of orthotropic functionally graded materials, Composites Part B, vol. 44, pp. 8–25, 2013.

[18] S.S. Hosseini, H. Bayesteh, and S. Mohammadi, Thermo-mechanical XFEM crack propagation analysis of functionally graded materials, Mater. Sci. Eng., vol. 561, pp. 285–302, 2013.

[19] E. Goli, H. Bayesteh, and S. Mohammadi, Mixed mode fracture analysis of adiabatic cracks in homogeneous and non-homogeneous materials in the framework of partition of unity and the path-independent interaction integral, Eng. Fract. Mech., vol. 131, pp. 100–127, 2014.

[20] T. Belytschko, Y.Y. Lu, and L. Gu, Element-free Galerkin methods, Int. J. Numer. Methods Eng., vol. 37, pp. 229–256, 1994.

[21] T. Belytschko, Y.Y. Lu, L. Gu, and M. Tabbara, Element-free Galerkin methods for static and dynamic fracture, Int. J. Solids Struct., vol. 32, pp. 2547–2570, 1995.

[22] T. Belytschko, Y.Y. Lu, and L. Gu, Crack propagation by element-free Galerkin methods, Eng. Fract. Mech., vol. 51, no. 2, pp. 295–315, 1995.

[23] T. Belytschko, Y. Krongauz, D. Organ, M. Fleming, and P. Krysl, Meshless methods: An overview and recent developments, Comput. Methods Appl. Mech. Eng., vol. 139, pp. 3–47, 1996.

[24] P. Krysl and T. Belytschko, Element-free Galerkin method: Convergence of the continuous and discontinuous shape functions, Comput. Methods Appl. Mech. Eng., vol. 148, pp. 257–277, 1997.

[25] S.S. Ghorashi, S. Mohammadi, and S.R.S. Yazdi, Orthotropic enriched element free Galerkin method for fracture analysis of composites, Eng. Fract. Mech., vol. 78, no. 9, pp. 1906–1927, 2011.

[26] U. Häussler-Combe and C. Korn, An adaptive approach with the element-free-Galerkin method, Comput. Methods Appl. Mech. Eng., vol. 162, pp. 203–222, 1998.

[27] V.P. Nguyen, T. Rabkzuk, S. Bordas, and M. Duflot, Meshless methods: A review and computer implementation aspects, Math. Comput. Simul., vol. 79, no. 3, pp. 763–813, 2008.

[28] S.N. Atluri and T. Zhu, A new meshless local Petrov-Galerkin (MLPG) approach in computational mechanics, Comput. Mech., vol. 22, pp. 117–127, 1998.

[29] S.N. Atluri, H.-G. Kim, and J.Y. Cho, A critical assessment of the truly meshless local Petrov-Galerkin (MLPG), and local boundary integral equation (LBIE) methods, Comput. Mech., vol. 24, pp. 348–372, 1999.

[30] S.N. Atluri and S. Shen, The meshless local Petrov-Galerkin (MLPG) method: A simple and less-costly alternative to the finite element and boundary element methods, Comput. Model. Eng. Sci., vol. 3, no. 1, pp. 11–51, 2002.

[31] E. Viola, F. Tornabene, E. Ferretti, and N. Fantuzzi, GDQFEM numerical simulations of continuous media with cracks and discontinuities, Comput. Model. Eng. Sci., vol. 94, no. 4, pp. 331–369, 2013.

[32] E. Viola, F. Tornabene, E. Ferretti, and N. Fantuzzi, On static analysis of composite plane state structures via GDQFEM and cell method, Comput. Model. Eng.Sci., vol. 94, no. 5, pp. 421–458, 2013.

[33] L. Sator, V. Sladek, and J. Sladek, Coupling effects in elastic analysis of FGM composite plates by mesh-free methods, Compos. Struct., vol. 115, pp. 100–110, 2014.

[34] V. Sladek, J. Sladek, and L. Sator, Physical decomposition of thin plate bending problems and their solution by mesh-free methods, Eng. Anal. Bound. Elem., vol. 37, no. 2, pp. 348–365, 2013.

[35] Y. Chen, J.D. Lee, and A. Eskandarian, Meshless Methods in Solid Mechanics, Springer-Verlag, New York, 2006.

[36] A. Asadpoure and S. Mohammadi, Developing new enrichment functions for crack simulation in orthotropic media by the extended finite element method, Int. J. Numer. Methods Eng., vol. 69, pp. 2150–2172, 2007.

[37] S.G. Lekhnitskii, Theory of an Anisotropic Elastic Body, Holden-Day, San Francisco, CA, 1963.

[38] G.C. Sih, P.C. Paris, and G.R. Irwin, On cracks in rectilinearly anisotropic bodies, Int. J. Fract. Mech., vol. 1, pp. 189–203, 1965.

[39] L. Guo, F. Guo, H. Yu, and L. Zhang, An interaction energy integral method for nonhomogeneous materials with interfaces under thermal loading, Int. J. Solids Struct., vol. 49, pp. 355–365, 2012.

[40] J.-H. Kim and G.H. Paulino, Mixed-mode fracture of orthotropic functionally graded materials using finite elements and the modified crack closure method, Eng. Fract. Mech., vol. 69, no. 14–16, pp. 1557–1586, 2002.

[41] P. Lancaster and K. Salkauskas, Surfaces generated by moving least squares methods, Math. Comput., vol. 37, pp. 141–158, 1981.

[42] G.R. Liu, Meshfree Methods Moving beyond the Finite Element Method, Second Edition, Taylor and Francis Group, LLC, Boca Raton, Florida, 2010.

[43] S. Mohammadi, Extended Finite Element Method for Fracture Analysis of Structures, First Edition, Blackwell Publishers, Oxford, UK, 2007.

[44] S. Mohammadi, XFEM Fracture Analysis of Composites, John Wiley & Sons, Ltd., Chichester, UK, 2012.

[45] J. Dolbow, An extended finite element method with discontinuous enrichment for applied mechanics, Ph.D. Thesis, Northwestern University, Evanston, IL, 1999.

[46] J.-H. Kim and G.H. Paulino, The interaction integral for fracture of orthotropic functionally graded materials: Evaluation of stress intensity factors, Int. J. Solids Struct., vol. 40, pp. 3967–4001, 2003.